Deep learning based characterization of human organoids using optical coherence tomography

Bingjie Wang[1], Razieh Ganjee[1], Irona Khandaker[1], Keevon Flohr[1], Yuanhang He[2,3], Guang Li[2], Joshua Wesalo[1], José-Alain Sahel[1], Susana da Silva[1,2,4], and Shaohua Pi[1,4*]

1 Department of Ophthalmology, University of Pittsburgh, Pittsburgh, PA 15213, USA
2 Department of Developmental Biology, University of Pittsburgh, Pittsburgh, PA, 15213, USA
3 School of Medicine, Tsinghua University, 100084, China
4 Department of Bioengineering, University of Pittsburgh, Pittsburgh, PA 15213, USA

**shaohua@pitt.edu*

Abstract: Organoids, derived from human induced pluripotent stem cells (hiPSCs), are intricate three-dimensional *in vitro* structures that mimic many key aspects of the complex morphology and functions of *in vivo* organs such as the retina and heart. Traditional histological methods, while crucial, often fall short in analyzing these dynamic structures due to their inherently static and destructive nature. In this study, we leveraged the capabilities of optical coherence tomography (OCT) for rapid, non-invasive imaging of both retinal, cerebral, and cardiac organoids. Complementing this, we developed a sophisticated deep learning approach to automatically segment the organoid tissues and their internal structures, such as hollows and chambers. Utilizing this advanced imaging and analysis platform, we quantitatively assessed critical parameters including size, area, volume, and cardiac beating, offering a comprehensive live characterization and classification of the organoids. These findings provide profound insights into the differentiation and developmental processes of organoids, positioning quantitative OCT imaging as a potentially transformative tool for future organoid research.

1. Introduction

Organoids, a groundbreaking development in tissue engineering and regenerative medicine, are three-dimensional cell cultures that closely replicate the structure and functionality of actual human organs [1-3]. These miniaturized organ analogs are usually cultivated from human induced pluripotent stem cells (hiPSC) through a complex *in vitro* differentiation process [4]. Occupying a distinct niche at the intersection of cell-based assays and *in vivo* animal models, human organoids strike a unique balance, offering physiological relevance akin to whole organisms while maintaining the experimental control of conditions. This reduced systemic complexity, as compared to full organisms, aids in streamlining data interpretation and isolating specific biological mechanisms or pathways. Human organoids have revolutionized research in key areas such as complex organ development, disease modeling, drug testing, and potential applications in organ transplantation, marking a significant stride in biomedical research and therapeutic development [5, 6].

Recently, human retinal organoids have become a focal point in vision research due to their ability to mimic many aspects of the human retina's structure and complexity [7-10]. These organoids, encompassing all necessary cell types, are instrumental in advancing our understanding of human retinal development, degeneration, and diseases such as age-related macular degeneration and retinitis pigmentosa, as well as other forms of inherited retinal dystrophies [11]. They are invaluable for developing and testing new treatments, such as gene

and cell therapies, offering a more relevant model than traditional 2D cultures. On a similar front, human cardiac organoids are revolutionizing cardiovascular research by replicating heart tissue properties and aiding in understanding heart diseases like cardiomyopathy and myocardial infarction, mimicking aspects of heart tissue, including its unique muscular and electrical properties [12-15]. They serve as crucial tools for investigating cardiac function and pathology. Overall, human retinal and cardiac organoids are at the forefront of developmental biology, stem cell technology, and tissue engineering, significantly advancing medical research.

However, the full potential of organoids is often limited by the lack of effective live imaging tools, particularly for 3D, longitudinal, and real-time assessments. Traditional histology, while detailed, falls short in imaging organoids due to its inability to monitor changes in the same samples, capturing only static snapshots of organoid growth and response to treatments. These limitations highlight the need for non-destructive imaging modalities capable of facilitating longitudinal studies and real-time monitoring of organoids, such as the OCT [16], a promising solution in this regard. In 2019, Elizabeth et al. used OCT for organoid assessments, aiming to reduce selection bias [17]. Dr. Kate Grieve's team advanced dynamic full-field OCT for noninvasive, living imaging of retinal organoids [18, 19]. Dr. Yoshiaki Yasuno's group leveraged OCT to study tissue dynamics in tumor and alveolar spheroids, providing insights into growth and behavior [20-23], while Dr. Chao Zhou's team focused on investigating cardiac organoid growth using OCT [24, 25]. The Vienna group applied ultra-high-resolution and multi-angle OCT for detailed organoid visualization [26, 27]. Collectively, these diverse applications highlight OCT's versatility in enabling high-resolution, rapid, and non-invasive evaluation of organoids in various research fields to advance our understanding of these complex 3D structures.

In this study, we utilized OCT imaging [28] to examine retinal, cerebral, and cardiac organoids. Significantly, we developed a deep learning network to segment the organoid tissues and their internal structures automatically. This enabled us to calculate quantitative biomarkers for morphological and functional analysis. Specifically, we distinguished retinal organoids from cerebroids, a differentiation by-product, based on the hollow structures. In cardiac organoids, we recorded their beating and correlated the number of chambers with their volume percentage. Overall, we anticipate that the integration of OCT and deep learning segmentation will contribute to precise quantifications, accelerating the pace of research for organoids.

2. Methods

2.1 Organoids

Differentiation of human retinal organoids (hRetOrg) procedure was based on previously described protocols [10, 29, 30], and cerebral organoids (cerebroids) were generated as by-products. Briefly, hiPSCs (line IMR90-4, WiCell) were dissociated to single cells using Accutase (Thermofisher Scientific, # 00-4555-56) and mechanical dissociation with a P1000 in 1-ml of mTeSR™ Plus (STEMCELL Technologies, #100-0276) containing 10-μM Rock inhibitor Y-27632 (STEMCELL Technologies, #72304). hiPSCs were then plated on 100-mm petri dishes (VWR # 25384-088) with a total volume of 10-ml mTeSR™ Plus to promote the formation of embryoid bodies (EBs). On Day (D) 1, approximately 1/3 of the medium was exchanged for neural induction medium (NIM) containing DMEM/F12 (Gibco, #11330057), 1% N2 supplement (Gibco, #17502048), 1x NEAAs (Sigma, #M7145), and 2-mg/ml heparin (Sigma, # H3149). On D2, approximately 1/2 of the medium was exchanged for NIM. On D3 EBs were plated in new 60-mm petri dishes (Corning #430166) in NIM. Half of the medium was changed every day until D6. At D6, BMP4 (R&D, #314-BP) was added to the culture at a final concentration of 1.5-nM. At D7, EBs were transferred to 60-mm dishes previously coated with Growth Factor-Reduced (GFR) Matrigel (Corning, #356230) and maintained with daily NIM changes until D15. On D16, NIM was exchanged for retinal differentiation medium (RDM) containing DMEM (Gibco, #15140122) and DMEM/F12 (1:1), 2% B27 supplement (without vitamin A, Gibco#12587-010), NEAAs, and 1% penicillin/streptomycin (Gibco,

#15140122). Feeding was done daily until D27. On D28, EBs were dislodged from the plate by checkerboard scraping, using a 10-µl or 200-µl pipette tip. Aggregates were washed three times and then maintained in 6 well culture plate (Greiner bio-one, #657185) in RDM medium. The medium was changed every 2-3 days. Feeding was done every 2-3 days, depending on the color of the medium. This protocol also generates cerebral organoids, or cerebroids, as by-products. Neural organoids were transferred from the incubator at different time points of differentiation (D31 to D136) for OCT imaging.

The cardiac organoid differentiation procedure was adapted from a protocol described previously [14, 31, 32]. Briefly, 1000 hiPSCs (the hiPSC line was generated from a healthy donor in the Li laboratory) were seeded in each well of ultra-low attachment 96-well plates (Fisher Scientific, #7201680). The cells were assembled into 3D structures by culturing in E8 medium for 5 days (day -5 to day 0). From day 0 to day 6, cells were cultured in RPMI supplemented with B-27 minus insulin. CHIR99021 at a final concentration of 11-µM was used on day 0 and lasted for 1 day. From day 3 to day 5, cells were treated with C59 at a final concentration of 2-µM. The cell aggregates were transferred to 5% Poly (2-hydroxyethyl methacrylate) (Sigma-Aldrich, P3932) coated 24 well tissue culture plates (Fisher Scientific, # 9761146) on day 7 and cultured in RPMI with B27 supplement until the end of differentiation. The fresh medium was changed every 2 days until tissue harvest. The VEGF was added to the culture media from day 3 to the end. On day 14 (D14), the cardiac organoids were transferred from the incubator for OCT imaging.

2.2 OCT Imaging Acquisition

The OCT imaging was performed with a visible light OCT (vis-OCT) prototype [28] developed at the University of Pittsburgh Department of Ophthalmology. The system covered a light spectrum (510 nm – 610 nm) from a supercontinuum laser (Super-K EXU-6, NKT Photonics), providing a 1.2-µm axial resolution in tissue. To image the organoids, a 2-D galvanometer scanner (Saturn 5B, Scanner Max) was used to steer the scanning beam, and a scan lens (LSM03-VIS, Thorlabs) was used to focus the light beam on the samples. The interferogram was spatially dispersed by an 1800 lines/mm transmission grating (Wasatch Photonics), detected by a line scan camera (spl4096-140km, Basler) with vertical and horizontal binning, and captured by a frame grabber (PCIe-1437, National Instruments). Hardware synchronization was achieved with a high-speed multifunction I/O device (PCIe-6353, National Instruments). The entire acquisition software was written in LabVIEW language with GPU acceleration. The image depth range was calibrated to 1.5-mm using microscope cover glass (12544D, Fisher Scientific). The field of view was calibrated using a 20 x 20 grid array with 100 µm pitch (R1L1S1N, Thorlabs).

To minimize the disturbance to the organoids, OCT scans were acquired while the organoids stayed at their original culture plate. Prior to OCT imaging, the samples were first examined and imaged by brightfield and phase contrast microscopy (EVOS M5000 Imaging System, Thermofisher Scientific). The samples were then transferred and placed on a 3-axis translation stage of the OCT system. The acquisition was performed at an A-line sampling rate of 50 kHz. Each raster scan consisted of 500×2 A-lines per B-scan and 500 B-scans, which finished in 10 seconds. The default field of view was set to 1×1-mm and changed to 2×2-mm if it was not enough to cover the large samples. For cardiac organoids, an additional M-B mode was used to quantify their beating in cross-sectional images. The beating scanning pattern consisted of 250 A-lines per B-scan (equivalent to 200 fps) and 4000 repetitive B-scans at the same position. For a typical heat beat rate (30~100 beats per minute), the scanning pattern can collect hundreds of data points to capture the detailed feature of the beating cycle, especially the peak pumping period which usually lasts less than a few tenths of the entire beating cycle. After imaging, each organoid was either returned to the incubator or proceeded for end-point histological analyses.

Following the experiment, the raw interferogram was transferred and processed in MATLAB to obtain the OCT images. The procedures include DC removal, dispersion

compensation, lambda-k linearization, and fast Fourier Transform (FFT). In the B-scans, organoid tissues appeared as bright areas with the background and organoid hollow/chamber appeared as dark areas inside the tissue. To enhance the contrast of organoids, we first applied a local brightening filter (*imlocalbrighten*) and followed with a median filter (*medfilt2*) to decrease speckle noise.

2.3 Deep Learning Segmentation

As the imaging was performed *in vitro* in a culture plate, the OCT images of human organoids may suffer from non-uniform intensity variation, ambiguous boundaries, and hyperreflective outliers (specular reflection) with similar intensity to tissues. In addition, tissues and hollows had different shapes, sizes, and locations in OCT B-scans. Therefore, accurate segmentation of these regions was a challenging task, calling for an efficient combination of local/low-level features like edges and texture, as well as global/high-level features like shape and size, to achieve a decent performance.

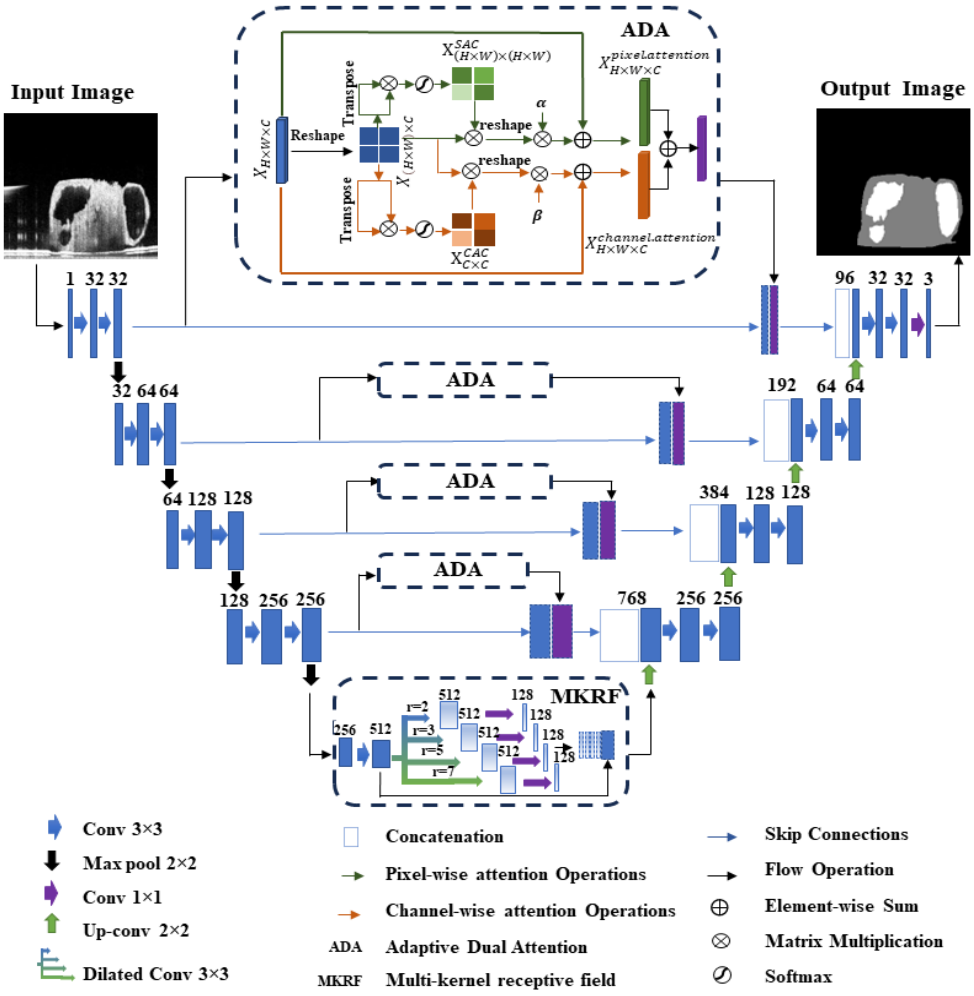

Fig.1. The architecture of the proposed OrgSegNet for deep learning segmentation of organoid tissue and inner structure in OCT B-scan images. A cardiac organoid is shown as a representative example.

Here, we developed a deep learning model, which we called OrgSegNet, dedicated to the segmentation of organoid tissue and internal structures. The framework of this model was built on the encoder-decoder architecture of U-Net [33] and was enriched by embedding an adaptive dual attention module (ADA) in skip connections, and a multi-kernel receptive field module (MKRF) within the gateway (Fig. 1). This architecture provides three specific benefits for accurate organoid segmentation: a) capture and fuse low-level and high-level features with the encoder-decoder structure, b) extract interdependencies of features adaptively in a long-range global view with the ADA modules to aggregate spatial/pixel and channel-wise attention in skip connections, c) demonstrate the larger and multi-scale field of view to capture more efficient global features by embedding the multi-kernel receptive field module in the gateway. The details of the ADA and MKRF modules are described below:

2.3.1 ADA module

Inspired by the attention strategy proposed in Ref. [34] with ResNet for scene image segmentation and several segmentation approaches that followed this attention mechanism [35-37], we proposed an ADA module (green and orange flow operations shown as the ADA module in Fig. 1) in our encoder-decoder-based segmentation model to improve the segmentation performance for the organoid images. This ADA module worked using the spatial/pixel and channel-wise attention mechanism. Firstly, the 3D encoder feature map output $X_{H\times W\times C}$ was reshaped into a 2D matrix $X_{(H\times W)\times C}$, where H, W, and C indicated the height, width, and channel sizes of feature maps, respectively. Secondly, the map of the spatial attention coefficients $X^{SAC}_{(H\times W)\times(H\times W)}$ was computed using Eq. (1) (green path in Fig. 1).

$$X^{SAC}_{(H\times W)\times(H\times W)} = softmax(X_{(H\times W)\times C}.X^{T}_{C\times(H\times W)}) \quad (1)$$

Where X^T indicated the transpose of X and '.' indicated the matrix multiplication. The coefficients were computed with a spatial correlation between any two pixels of X and X^T, and then a softmax function for the probability value of each correlation score. The higher correlations were obtained, the greater probability was assigned to the positions. After that, the weights of spatial attention were multiplied by the input feature map $X_{(H\times W)\times C}$, reshaped back to matrix with $H\times W\times C$ dimension, multiplied to score parameter α, and added to the encoder feature map output $X_{H\times W\times C}$ to obtain pixel-wise attention map $X^{pixel.attention}_{H\times W\times C}$ as Eq. (2), where each pixel element was a weighted sum of highlighted features with original input features to boost extraction of local features across spatial positions.

$$X^{pixel.attention}_{H\times W\times C} = \alpha \times (reshape(X^{SAC}_{(H\times W)\times(H\times W)}.X_{(H\times W)\times C})) + X_{H\times W\times C} \quad (2)$$

The flow operation of computing the channel-wise attention $X^{channel.attention}_{H\times W\times C}$ (orange path in ADA module of Fig. 1) was similar to the pixel-wise attention with slight modifications. The equations to calculate channel attention coefficients $X^{CAC}_{C\times C}$ and channel-wise attention feature $X^{channel.attention}_{H\times W\times C}$ were as below:

$$X^{CAC}_{C\times C} = softmax(X^{T}_{C\times(H\times W)}.X_{(H\times W)\times C}) \quad (3)$$

$$X^{channel.attention}_{H\times W\times C} = \beta \times (reshape(X_{(H\times W)\times C}.X^{CAC}_{C\times C})) + X_{H\times W\times C} \quad (4)$$

The adaptive parameters α and β were set to zero initially and learned by the model during the training phase to adaptively enrich local features with their global dependencies across positions and channels. At the end of the ADA module, these spatial and channel-wise attention coefficients were fused with an element-wise sum, combining the benefit from both attention mechanisms where the values of each local feature map were updated with a weighted sum of original features and interdependencies of features independent of their position and channel.

These enriched features were concatenated to the original input features in the encoder and transferred to the corresponding decoder layer for further processing.

2.3.2 MKRF module

The local information is prone to fade, and global information is prone to be highlighted in the terminal layers of the proposed model due to a decrease of spatial resolution. Inspired by atrous pyramid pooling [38, 39], we enriched the global feature maps in the gateway layer by proposing a multi-kernel receptive filed module consisting of 4 dilated convolutions with dilation rates $r = 2, 3, 5, 7$ as (Eq. 5)

$$y[i] = \sum_k x[i + rk]w[k] \quad (5)$$

Where x, w, and y indicated the input feature map, convolution filter, and output feature map, respectively. r was a dilation rate determining the number of added zero values between two consecutive filters in each spatial dimension. This module assisted the model in learning contextual features efficiently without further reducing spatial resolution. As shown in the gateway layer in Fig. 1, the multi-scale dilated convolutions with r=2, 3, 5, and 7 encoded global information with four receptive field sizes 5×5, 7×7, 11×11, and 15×15, respectively. The dimension of these feature maps was reduced to C/4 by passing them through four 1×1 standard convolutions, where C was the channel number of the original input feature map. Finally, the results were concatenated with the original global features and transferred to the corresponding decoder layer.

2.3.3 Training and validation

The model was trained with a set of B-scan images (N=4000), including both the retinal, cerebral and cardiac organoids. The ground truth of tissue and inner structure were manually delineated by experienced graders. The training set was further enlarged with data augmentation including contrast adjustment, random rotations, and transpose. The hyperparameters during training included learning rate (2e-3), batch size=4, epochs number=20, and RMSprop optimizer. A combination of Dice and Bicon loss [40] was used as a loss function. The model was implemented in Python 3.9 and TensorFlow v2.8.0 platforms with NVIDIA GeForce RTX 4060 Ti and 64 GB of RAM.

As shown in Fig. 2, the OrgSegNet segmented the organoid samples successfully. The network demonstrated excellent tolerance for strong specular reflection, affecting neither the segmentation of tissue nor the inner structure (yellows arrows in Fig. 2). The bottom supporting membrane of the culture plate, which had strong reflectance, was also successfully excluded from tissue segmentations (green arrow in Fig. 2). Additionally, as the reflectance attenuated significantly along depth due to the opacity of the samples (especially for the cardiac organoids, magenta arrows in Fig. 2), their inner structure (chamber) was not so remarkable to the tissue, sometimes cannot be determined/identified during manual delineation (orange arrow in Fig 2 C). However, the algorithm avoided classifying significantly attenuated tissue regions as hollow (chamber) and were able to highlight inner structures that were neglected (or hard to determine) during manual delineation.

Recall, precision, and dice coefficient (DIC) measurements were used for the evaluation with k=3 cross-validation (Table 1). The accuracy of segmentations in both tissue and inner structure were very high (>0.96 for tissue and >0.91 for inner structure). We noticed lower segmentation performance in the hollow (chamber) than the tissue, which can be anticipated due to the discrepancy between the ground truth and deep learning results (inset in Fig. 2 C) for images like Fig. 2 C that delineating and distinguishing the correct boundary of the hollow was challenging during manual inspection while the OrgSegNet helped identify these challenging inner structures.

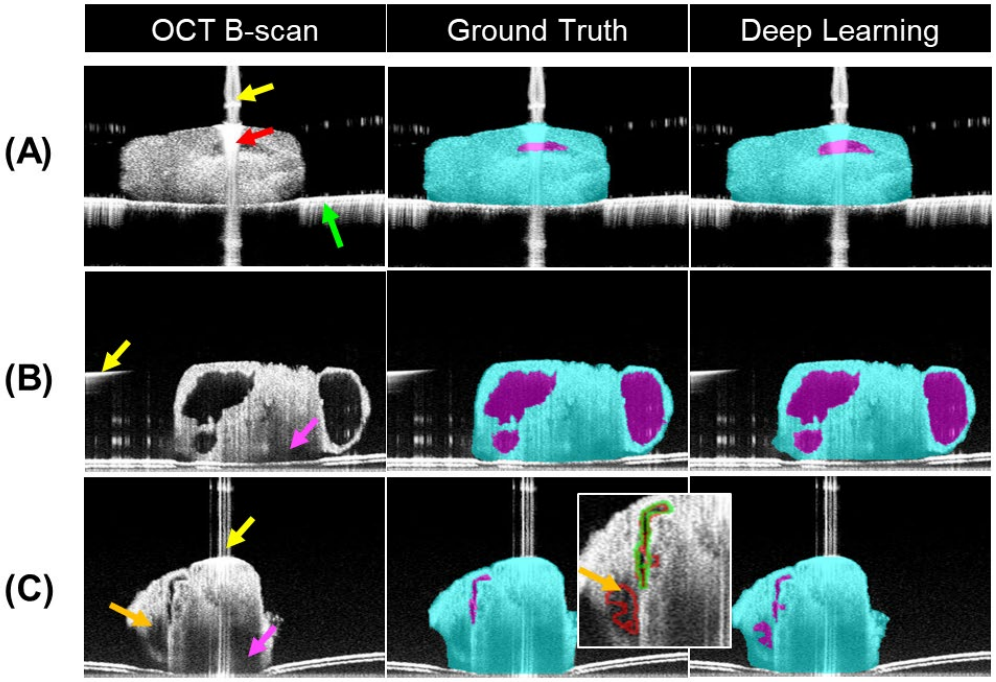

Fig.2. Representative OCT B-scan images of human organoids, the ground truth of binary images, and subsequent segmentations using OrgSegNet. Tissue segmentation is in cyan and hollows in magenta. Arrows indicate the challenging conditions for segmentation including specular reflection (yellow and red), base membrane of culture plate (green), reflectance attenuation (magenta), and ambiguous inner structure (orange). The zoom-in overlay of hollow segmentations on panel C inset demonstrated representative cases causing a discrepancy between the ground truth (green color) and deep learning (red color) results where the OrgSegNet highlighted the regions that are challenging in manual delineation.

Table 1. Evaluation of deep learning segmentation performance on organoids.

	Recall	Precision	Dice
Tissue	0.968±0.106	0.965±0.095	0.983±0.060
Hollow (Chamber)	0.944±0.117	0.917±0.178	0.919±0.177

2.4 Quantitative Biomarkers

With accurate and automated segmentation results, quantifications could be conducted to obtain the features of the organoids. For each organoid, we calculated the size (unit: mm), area (unit: mm^2), tissue volume (V_{Tissue}, unit: mm^3), hollow (chamber) volume (V_{Hollow}, unit: nL), and the ratio of hollow to tissue volume (unit: %). The size and area of organoid were determined by the maximal caliber in the axial direction and the area of region occupied by the organoids in the projected *en face* images, respectively. With the volumetric binary mask of the inner structure, we were able to determine if connectivity of compartments, and therefore, count their numbers. This is challenging in traditional 2-D images as the organoids are 3-D structure. A cutoff (0.01 nL, equivalent to 500 voxels) of inner structure volume was used to determine the chamber number of organoids in this study. Additionally, for cardiac organoids, we were able to observe their beating and calculate their beat cycle (unit: s), beat rate (unit: bpm), pulsation displacement (unit: μm), and pulsation enlargement (unit: %). The pulsation displacement was defined as the maximal shift of the tissue surface during the beating cycle. The pulsation enlargement was defined as the maximal change of tissue area.

2.5 Immunostaining Validation

hRetOrg and cerebroids were fixed with 4% PFA at RT for 30 min and washed 3 times with PBS. Subsequently, the organoids were cryoprotected in 1x PBS-30% sucrose at 4°C O/N. The next day, organoids were pre-embedded in a mixture of sucrose (1:1) for 30 minutes to 1 hour on ice and embedded in individual blocks in dry-iced 90% ethanol. Cryosections of 16 µm thickness were collected on Superfrost Plus slides (Fisher, #12-550-15). Once fully dried, slides were stored at -80°C until further processing. On the day of staining, slides were removed from -80°C and allowed to warm up to RT for approximately 20 min. Slides were washed 3 times with PBS and blocked 1 h at RT with 5% Donkey Serum and 0.1% Triton X-100 in 1x PBS. Primary antibodies were diluted in 2% Donkey Serum in PBS and incubated at 4°C O/N. Primary antibodies used included anti-Rhodopsin (Millipore, cat# MAB5356, 1:100 dilution), anti-M/L cone (Millipore, cat# AB5405, 1:200 dilution), anti-CTIP2 (Abcam, #ab18465, 1:300 dilution), and anti-FOXG1 (Invitrogen, #702554, 1:150 dilution). Slides were rinsed 3 times, 5-min each, with 1x PBS. Appropriate secondary antibodies (Thermofisher; 1:500 dilution) were added and incubated for 1 hour at RT, followed by 3 rinses with PBS, 5-min each. The slides were counterstained with Hoechst at RT for 5-min and further washed twice before mounting with Fluoromount-G solution (Southern Biotech, #0100-01). Slides were imaged using a Leica Thunder system microscope.

2.6 Statistics

The Shapiro-Wilk test was performed to assess the normality of quantitative features. Two-sample t-tests were used to determine the significance ($p<0.05$) for size, area, and volume between retinal organoid and cerebroid. The Mann-Whitney *U* tests were used to compare hollow volume and ratio to total volume between the two groups. Spearman correlation analysis was adopted to determine the association between the parameters among the same group. An exponential curve was used to fit the relationship between the number of chambers and the chamber-to-tissue ratio in cardiac organoids. The data were presented as mean ± standard deviation (SD). P-values smaller than 0.01 were considered statistically significant. All statistical analysis was conducted using SPSS 28.0 (IBM Corporation, Chicago, IL).

3. Results

3.1 Retinal Organoids

3.1.1 Appearance and Quantification with OCT

Live hRetOrg (N=11) at various developmental stages (D31-D136) were successfully imaged with the high-resolution vis-OCT system. These organoids, with their detailed top and bottom surfaces, were confidently visualized through volumetric rendering (Fig. 3). The neural retina's reflective nature was evident at these stages, revealing a thick pseudo-stratified layer in both *en face* and B-scan OCT images, corresponding to bright-field and phase contrast microscopy observations (Fig. 3 A). Immunostaining at D117 confirmed the presence of photoreceptors (PRs) on the outermost side of the organoids (Fig. 3 B), whereas retinal ganglion cells (RGCs) were located in the innermost side of the neuroretina. However, these cell types lacked the uniform orientation necessary to form the multi-layer lamination structure, which was found in the *in vivo* retina. Additionally, retinal pigment epithelium (RPE) cells were either absent or concentrated adjacent to the neural retina (Fig. 3 C), blocking the probe light penetrating underneath the structure, casting strong shadows in OCT images, and therefore demonstrating enhanced contrast in OCT *en face* images compared to traditional microscopy.

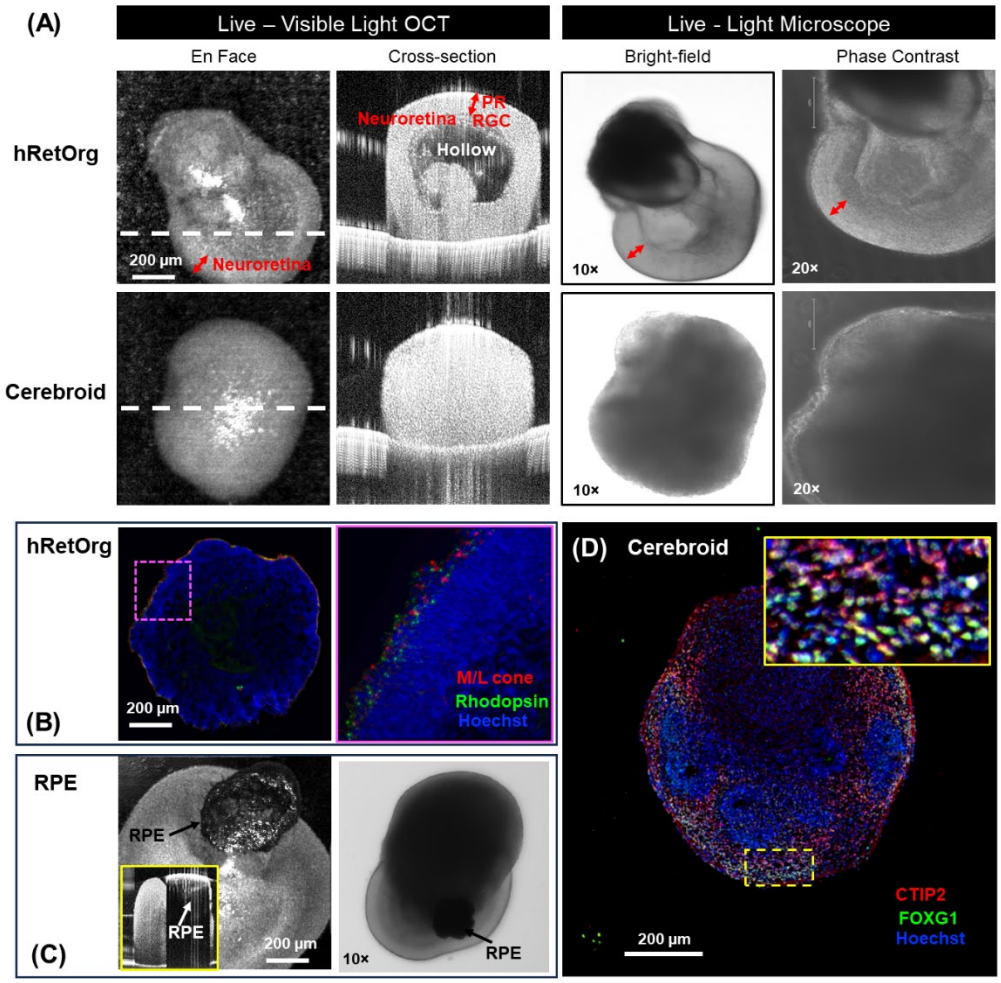

Fig.3. Representative images of hRetOrg and cerebroids at different time points of development. (A) Live hRetOrg and cerebroid at day (D) D31 in OCT and microscopy. Note the presence of neuroretina lamination and hollow structure in hRetOrg but not in the cerebroids, which were more evident in OCT B-scans. (B) hRetOrg at D117 immuno-stained for M/L cones and rods counterstained with Hoechst. Note the location of these photoreceptor cells at the outer edge of the hRetOrg. (C) OCT and microscopy images of a hRetOrg with RPE (arrows). Note the presence of a strong shadow on OCT scans corresponding to RPE (white arrow). (D) Cerebroid at D60 immuno-stained for the cerebral markers FOXG1 and CTIP2 counterstained with Hoechst. PR, photoreceptors; RGC, retinal ganglion cells; RPE, retinal pigment epithelium.

The average size, area, and volume of hRetOrg were measured as 0.49 ± 0.14 mm, 0.79 ± 0.35 mm^2, and 0.26 ± 0.13 mm^3 respectively (Fig. 4, Table 2). The volume was highly correlated to the area (R=0.88, *p*-value <0.01), while not to the size (R=0.28, *p*-value=0.40). Notably, the majority of hRetOrgs (10 out of 11) featured significant hollow or semi-hollow centers with low reflectivity, contrasting the bright neuroretina (Fig. 3 A). These hollows, being optical clear and lacking neuronal structure (Fig. 3 B), accounted for an average volume of 11.58 ± 14.91 nL (Fig. 4 C), or 4.15% ± 3.99% of the total organoid volume, and were independent to the organoid tissue volume with no correlation (R=0.36, *p*-value=0.29).

3.1.2 Classification to cerebroids

Cerebroids are differentiated as by-products in current hRetOrg protocols. Therefore, existing culture methods for hRetOrg required lengthy steps of manual trimming and selection.

Although denser and opaquer under the microscope, their appearance was similar to hRetOrg, making the identification and trimming challenging. OCT imaging of cerebroids (N=17, verified with immunostaining, Fig. 3D) from the same developmental time points as hRetOrg, revealed similar size (0.45 ± 0.15 mm, *p*-value=0.35) and volume (0.39 ± 0.23 mm^3, *p*-value=0.10), but absence of hollow structures (0 for manual ground truth, 0.03 ± 0.07 nL for deep learning segmentation, *p*-value<0.01) compared to hRetOrg (Fig. 4 and Table 2). Additionally, the cerebroid demonstrated a more regular (sphere) shape, as validated with a high correlation coefficient (R=0.84, *p*-value<0.01) between their volume and size. The area under the receiver operating characteristic (ROC) curve (AROC) in distinguishing hRetOrg from cerebroids based on the hollow structure was over 0.99 (Fig. 4F), which was significantly higher than that using tissue volume (AROC=0.69), indicating excellent automated and unbiased classification performance.

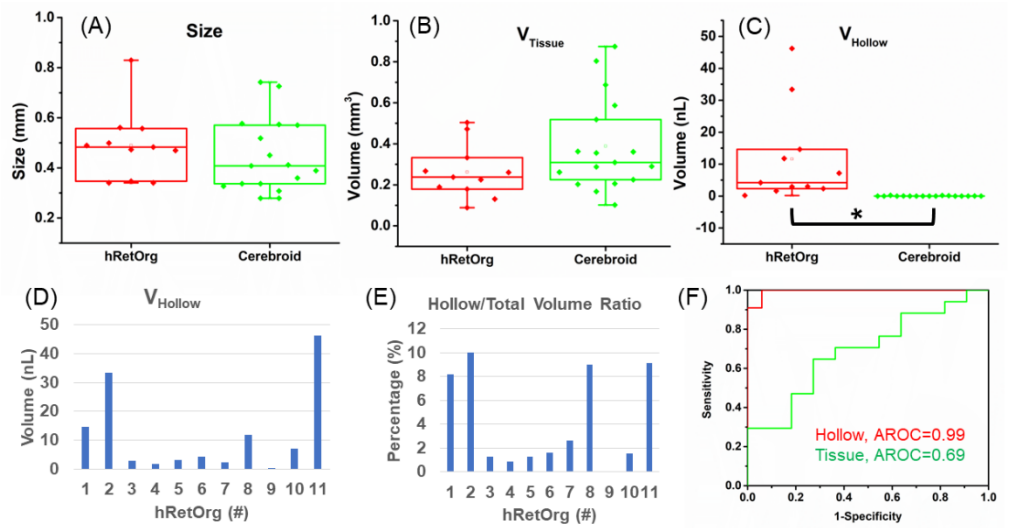

Fig.4. hRetOrg and cerebroid quantitative features extracted from OCT images and OrgSegNet platform. (A) – (C) Comparison between hRetOrg (red) and cerebroid size (green) (A), tissue volume (B) and hollow volume (C). '*' indicated the significance of the hollow structure between hRetOrg and cerebroid. (D) – (E) Hollow volume (D), and ratio of hollow per total organoid volume (E) for each individual hRetOrg sample. (F) The area under the receiver operating characteristic (ROC) curve (AROC) performance (F) distinguishing hRetOrg from cerebroid based on hollow structure was 0.99, much higher than 0.69 based on tissue volume.

Table 2. Quantitative features of hRetOrg and cerebroids obtained from quantitative OCT imaging.

	Sample (N)	Size (mm)	Area (mm^2)	V_T (mm^3)	V_H (nL)	$R_{H/T}$ (%)
hRetOrg	11	0.49±0.14	0.79±0.35	0.26±0.13	11.58±14.91	4.15±3.99
Cerebroid	17	0.45±0.15	1.12±0.39	0.39±0.23	0.03 ± 0.07	0.01±0.02

3.2 Cardiac Organoids

3.2.1 Appearance and Quantification with OCT

Cardiac organoids (N=7), as visualized by vis-OCT, displayed an irregular shape (Fig. 5 A) with bright reflectance and significant signal attenuation along their depth (Fig. 5 B). This

attenuation may result from the cardiac tissue's lower transparency. Their size (0.39 ± 0.02 mm) and volume (0.38 ± 0.06 mm^3) were similar or smaller compared to retinal organoids.

3.2.2 Chambers

All cardiac organoids featured chambers, appearing as weakly reflective spaces in OCT images (Fig. 5 B). These chambers were larger (58.94 ± 54.98 nL) and occupied a greater proportion (14.34% ± 11.86%) of the organoid compared to those in hRetOrg. With the 3-D segmentation of the chambers, we were able to count the number of chambers. We observed multiple chambers in these organoids (average 8 ± 4) (Fig. 5 B and C) and found an exponential relationship between the volume percentage of the chambers and their number ($C/T = 34.82 \times e^{-0.156N}$, R^2=0.82) (Fig. 5 D), indicating a potential tendency for chambers to merge during development. A predominant chamber, accounting for 73.26% ± 17.90% of all chamber volumes, supported this hypothesis.

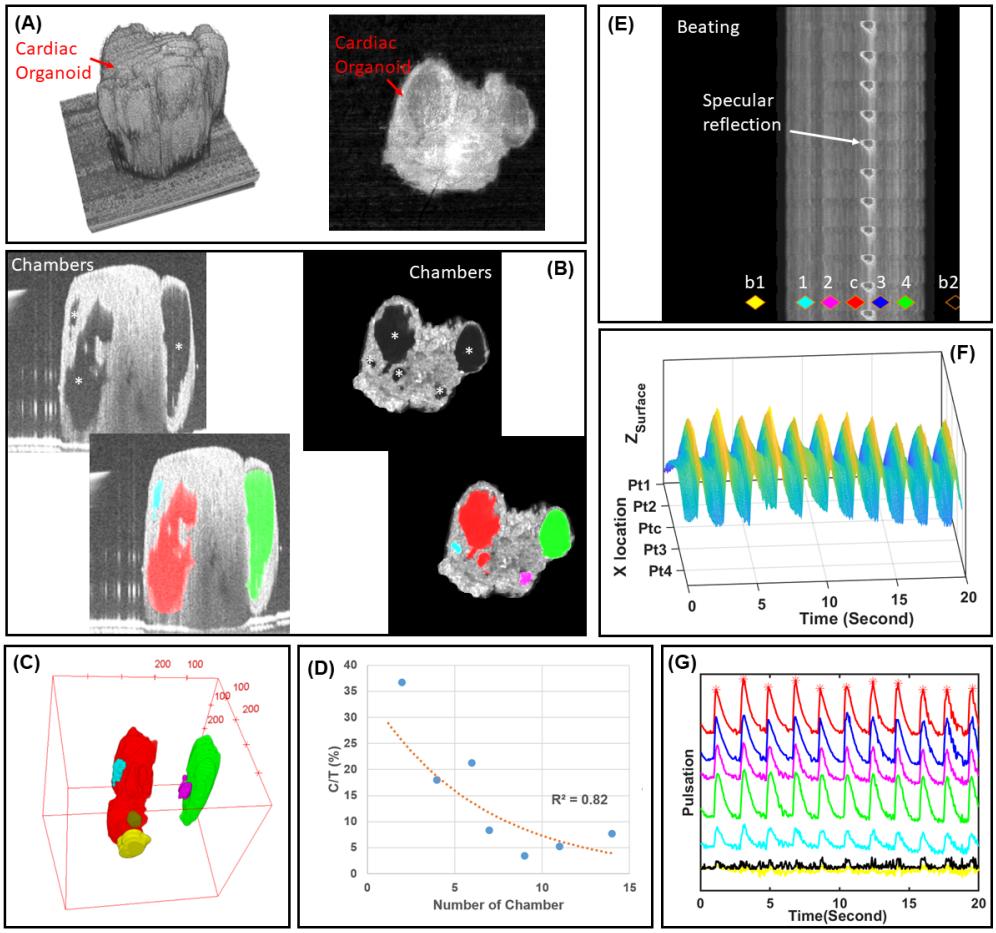

Fig.5. (A) The 3D and projected *en face* visualization of a cardiac organoid by OCT. (B) cross-sectional and depth plane visualization of chambers (marked with stars) in cardiac organoids, as well as their segmentations. Each isolated chamber was assigned a different color. (C) 3D visualization of the segmented chambers of cardiac organoid. (D) The association of the number of chambers with the percentage of chamber to total volume. An exponential fitting ($C/T = 34.82 \times e^{-0.156N}$) was performed with an R-square of 0.82. (E) Projected *en face* image of an OCT beating scan for cardiac organoids. Note the occasional specular reflection due to the movement. (F) Appreciation of the cardiac beating by the axial position of detected organoid tissue surface. (G) Appreciation of the cardiac beating by examination of the axial position in specific locations

of organoids (point c and 1-4 in E), in contrast to the static background board (point b1 and b2 in E).

3.2.3 Cardiac beating

The beating motion of cardiac organoids was captured by OCT M-B-scan images at the same cross-section. Cardiac motion altered light propagation, leading to periodic specular reflections at same locations. (Fig. 5 E). The area of organoid tissue periodically changed due to beating, indicating a 3.84% ± 2.04% enlargement during beating. Displacement (16.22 μm ± 7.85 μm) varied across different locations (Fig. 5 G). By identifying the time points with peak values for the displacement, we determined the beat cycle and rate as 1.72 s ± 0.16 s and 35.50 ± 3.51 bpm, respectively.

Table 3. Statistical features of cardiac organoids obtained from quantitative OCT imaging.

Measurement of Cardiac Organoid	
Size (mm)	0.39±0.02
Area (mm^2)	1.14±0.21
Volume (mm^3)	0.38±0.06
Chamber Number (N)	8±4
Chamber Volume (nL)	58.94±54.98
Max / All Chamber (%)	73.26±17.90
Chamber / Total Volume (%)	14.34±11.86
Beat Cycle (s)	1.72±0.16
Beat Rate (bpm)	35.50±3.51
Pulsation Displacement (μm)	16.22±7.85
Pulsation Enlargement (%)	3.84±2.04

4. Discussion

In this study, we employed noninvasive, 3D OCT imaging for human organoids, highlighting its advantages over traditional histological methods (requiring tissue fixation, sectioning, and staining). OCT's non-destructive nature [24, 41] is pivotal for observing dynamic biological processes and long-term organoid development [24, 42, 43]. Its capability for rapid, real-time, high-resolution, 3D imaging surpasses the time-consuming and labor-intensive nature of traditional 2D histology, providing a more complete understanding of whole organoid architecture.

Significantly, we developed OrgSegNet, a deep learning network, to perform automated, quantitative OCT imaging of organoids. This model employs novel adaptive dual attention and multi-kernel receptive field strategies to effectively segment both tissue and hollow (chamber) structures. To the best of our knowledge, OrgSegNet stands out as the first deep learning network dedicated to segmenting 3-D organoid tissue and inner structure automatically in OCT images [42, 44], providing a novel high-level morphological characterization technique to the field of organoids. OrgSegNet demonstrated robust segmentation performance across retinal, cerebral, and heart organoids with a single training process, reducing human error and bias in image interpretation. This feature is vital for reliable organoid characterization, which is essential for large-scale studies and tracking changes over time [45].

The quantitative measurements offer precise data on the morphological characteristics of organoids. For instance, using the hollow as a feature [17], we successfully distinguished hRetOrg from cerebroids. This distinction is relevant for several reasons. First, accurate classification ensures the purity of hRetOrg cultures. Since hRetOrg is used to model retinal development and disease, any contamination with cerebroids can confound experimental results in the validity and reproducibility of research findings. Second, distinguishing hRetOrg from cerebroids allows for more efficient use of resources as culturing human organoids is a

resource-intensive process, requiring significant time, materials, and financial investment. Identifying and segregating non-retinal tissues early in the process helps in directing resources toward the most promising specimens for further development and study, thereby improving the cost-effectiveness of the research. Finally, for hRetOrg to be considered for therapeutic applications [46], such as disease modeling, drug screening, or even cell replacement therapies, they must be free from non-retinal cells that could introduce unwanted variables or adverse effects. Clear classification is therefore critical in the context of translational medicine, where the ultimate goal is to develop safe and effective treatments for retinal diseases.

For cardiac organoids, the ability to accurately measure beating parameters, such as beat rate and pulsation displacement, represents a significant leap in understanding the functional dynamics of these miniature heart models [25]. These parameters offer a direct insight into the physiological state of the organoids, extending beyond mere structural analysis to encompass the functional vitality and responsiveness of the organoid tissue. The beat rate, a critical indicator of cardiac health, can reflect the organoid's maturity and its similarity to *in vivo* heart tissue, providing a real-time assessment of cardiac functionality. Pulsation displacement, on the other hand, offers a measure of the contractile strength and rhythmicity of the organoid, which is essential for understanding cardiac mechanics at a microscale. Crucially, these functional biomarkers open up possibilities for high-throughput screening of cardiac drug efficacy and safety. For instance, changes in beat rate or rhythm in response to pharmacological agents can signal potential cardiotoxic effects, a primary concern in drug development [47]. Conversely, improvements in these parameters might indicate therapeutic benefits, especially in the context of regenerative medicine or genetic therapies targeting cardiac conditions [14, 48]. This capability to quantitatively assess cardiac function *in vitro* provides a valuable tool for drug discovery, allowing for early detection of adverse cardiac effects and the optimization of therapeutic strategies. Additionally, in genetic studies, alterations in these beating parameters can help elucidate the roles of specific genes in cardiac development and disease [32]. In summary, the measurement of beating parameters in cardiac organoids offers a comprehensive functional assessment, bridging the gap between cellular models and whole-heart physiology, and holds great promise for advancing cardiac research and pharmaceutical development.

However, our study faces limitations. One primary limitation of our study is the potential specificity of the deep learning algorithm, OrgSegNet, to the types of organoids studied—retinal, cerebral, and cardiac organoids. The unique morphological and functional characteristics of different organoid types may require distinct algorithmic approaches or adaptations of the existing model, raising questions about the scalability and adaptability of the method to a broader range of organoid systems, especially the deep layers of larger or denser samples that OCT have limited depth penetration. Additionally, the accuracy of deep learning models heavily relies on the quality of ground truth data, which often requires expert manual annotation, a time-consuming and potentially biased process. Future development of annotation-free methods might be of high interest. Furthermore, while the current method provides decent morphological and functional insights, it might not capture certain cellular or sub-cellular details that are crucial for some research purposes, pointing towards the need for more functional measurements [18, 22], and/or the integration with other imaging modalities, such as fluorescence microscopy or electron microscopy, to achieve a more comprehensive organoid characterization. This integration could provide a multi-scale understanding of organoids, from macroscopic structure and function to microscopic cellular details. Lastly, the application of this technology in clinical settings (such as cell transplantation) or more complex organoid systems, such as those involving multiple organ types or organ-on-a-chip models [49], remains to be explored. These future applications would not only enhance our understanding of human organ development and disease but also open new avenues in personalized medicine and drug testing. Therefore, addressing these limitations and exploring these future directions will be crucial for realizing the full potential of OCT and deep learning in organoid research and beyond.

5. Conclusion

In conclusion, OCT imaging combined with deep learning represents a significant advancement in organoid research, allowing precise quantification of biomarkers like size, volume, and beating dynamics. These technologies may offer a standardized approach to organoid characterization, facilitating comparisons across studies and enhancing our understanding in areas such as developmental biology, disease modeling, and regenerative medicine.

Acknowledgments

We appreciate the funding from the Knight Templar Eye Foundation (SP and SdS), Alcon Research Institute (SP), and Eye & Ear Foundation of Pittsburgh (SP and BW). We are thankful to have benefited from the ARVO Foundation for Eye Research, specifically the ARVO/Genentech AMD Research Fellowship Grant and NIH R01 grant (EY033385) awarded to Dr. Susana da Silva and NIH DP2 grant (HL163745) to Guang Li. We also acknowledge support from NIH CORE Grant P30 EY08098 and an unrestricted grant from Research to Prevent Blindness to the Department of Ophthalmology.

Disclosures

The authors declare no conflicts of interest.

Data availability

Data underlying the results presented in this paper are not publicly available at this time but may be obtained from the authors upon reasonable request.

References

1. S. Alhaque, M. Themis, and H. Rashidi, "Three-dimensional cell culture: from evolution to revolution," Philosophical Transactions of the Royal Society B: Biological Sciences **373**, 20170216 (2018).
2. N. Akkerman, and L. H. Defize, "Dawn of the organoid era: 3D tissue and organ cultures revolutionize the study of development, disease, and regeneration," Bioessays **39**, 1600244 (2017).
3. J. y. Shoji, R. P. Davis, C. L. Mummery, and S. Krauss, "Global meta-analysis of organoid and organ-on-chip research," Advanced Healthcare Materials, 2301067 (2023).
4. C. Liu, A. Oikonomopoulos, N. Sayed, and J. C. Wu, "Modeling human diseases with induced pluripotent stem cells: from 2D to 3D and beyond," Development **145**, dev156166 (2018).
5. T. Takahashi, "Organoids for drug discovery and personalized medicine," Annual review of pharmacology and toxicology **59**, 447-462 (2019).
6. G. S. P. Hsia, J. Esposito, L. A. da Rocha, S. L. G. Ramos, and O. K. Okamoto, "Clinical application of human induced pluripotent stem cell-derived organoids as an alternative to organ transplantation," Stem cells international **2021**, 1-16 (2021).
7. M. O'Hara-Wright, and A. Gonzalez-Cordero, "Retinal organoids: a window into human retinal development," Development **147**, dev189746 (2020).
8. S. Kim, A. Lowe, R. Dharmat, S. Lee, L. A. Owen, J. Wang, A. Shakoor, Y. Li, D. J. Morgan, and A. A. Hejazi, "Generation, transcriptome profiling, and functional validation of cone-rich human retinal organoids," Proceedings of the National Academy of Sciences **116**, 10824-10833 (2019).
9. K. C. Eldred, S. E. Hadyniak, K. A. Hussey, B. Brenerman, P.-W. Zhang, X. Chamling, V. M. Sluch, D. S. Welsbie, S. Hattar, and J. Taylor, "Thyroid hormone signaling specifies cone subtypes in human retinal organoids," Science **362**, eaau6348 (2018).
10. T. Nakano, S. Ando, N. Takata, M. Kawada, K. Muguruma, K. Sekiguchi, K. Saito, S. Yonemura, M. Eiraku, and Y. Sasai, "Self-formation of optic cups and storable stratified neural retina from human ESCs," Cell stem cell **10**, 771-785 (2012).
11. G. Gagliardi, K. B. M'Barek, and O. Goureau, "Photoreceptor cell replacement in macular degeneration and retinitis pigmentosa: a pluripotent stem cell-based approach," Progress in retinal and eye research **71**, 1-25 (2019).
12. D. J. Richards, Y. Li, C. M. Kerr, J. Yao, G. C. Beeson, R. C. Coyle, X. Chen, J. Jia, B. Damon, and R. Wilson, "Human cardiac organoids for the modelling of myocardial infarction and drug cardiotoxicity," Nature Biomedical Engineering **4**, 446-462 (2020).
13. B. Nugraha, M. F. Buono, L. von Boehmer, S. P. Hoerstrup, and M. Y. Emmert, "Human cardiac organoids for disease modeling," Clinical Pharmacology & Therapeutics **105**, 79-85 (2019).
14. Y. R. Lewis-Israeli, A. H. Wasserman, M. A. Gabalski, B. D. Volmert, Y. Ming, K. A. Ball, W. Yang, J. Zou, G. Ni, and N. Pajares, "Self-assembling human heart organoids for the modeling of cardiac development and congenital heart disease," Nature communications **12**, 5142 (2021).
15. S. Jiang, W. Feng, C. Chang, and G. Li, "Modeling human heart development and congenital defects using organoids: How close are we?," Journal of Cardiovascular Development and Disease **9**, 125 (2022).

16. D. Huang, E. A. Swanson, C. P. Lin, J. S. Schuman, W. G. Stinson, W. Chang, M. R. Hee, T. Flotte, K. Gregory, C. A. Puliafito, and J. G. Fujimoto, "Optical coherence tomography," Science **254**, 1178-1181 (1991).
17. E. E. Capowski, K. Samimi, S. J. Mayerl, M. J. Phillips, I. Pinilla, S. E. Howden, J. Saha, A. D. Jansen, K. L. Edwards, and L. D. Jager, "Reproducibility and staging of 3D human retinal organoids across multiple pluripotent stem cell lines," Development **146**, dev171686 (2019).
18. J. Scholler, K. Groux, O. Goureau, J.-A. Sahel, M. Fink, S. Reichman, C. Boccara, and K. Grieve, "Dynamic full-field optical coherence tomography: 3D live-imaging of retinal organoids," Light: Science & Applications **9**, 140 (2020).
19. K. Groux, A. Verschueren, C. Nanteau, M. Clémençon, M. Fink, J.-A. Sahel, C. Boccara, M. Paques, S. Reichman, and K. Grieve, "Dynamic full-field optical coherence tomography allows live imaging of retinal pigment epithelium stress model," Communications Biology **5**, 575 (2022).
20. I. Abd El-Sadek, A. Miyazawa, L. T.-W. Shen, S. Makita, S. Fukuda, T. Yamashita, Y. Oka, P. Mukherjee, S. Matsusaka, and T. Oshika, "Optical coherence tomography-based tissue dynamics imaging for longitudinal and drug response evaluation of tumor spheroids," Biomedical Optics Express **11**, 6231-6248 (2020).
21. I. Abd El-Sadek, A. Miyazawa, L. T.-W. Shen, S. Makita, P. Mukherjee, A. Lichtenegger, S. Matsusaka, and Y. Yasuno, "Three-dimensional dynamics optical coherence tomography for tumor spheroid evaluation," Biomedical optics express **12**, 6844-6863 (2021).
22. I. Abd El-Sadek, L. T.-W. Shen, T. Mori, S. Makita, P. Mukherjee, A. Lichtenegger, S. Matsusaka, and Y. Yasuno, "Label-free drug response evaluation of human derived tumor spheroids using three-dimensional dynamic optical coherence tomography," Scientific Reports **13**, 15377 (2023).
23. R. Morishita, T. Suzuki, P. Mukherjee, I. Abd El-Sadek, Y. Lim, A. Lichtenegger, S. Makita, K. Tomita, Y. Yamamoto, and T. Nagamoto, "Label-free intratissue activity imaging of alveolar organoids with dynamic optical coherence tomography," Biomedical Optics Express **14**, 2333-2351 (2023).
24. Y. Ming, S. Hao, F. Wang, Y. R. Lewis-Israeli, B. D. Volmert, Z. Xu, A. Goestenkors, A. Aguirre, and C. Zhou, "Longitudinal morphological and functional characterization of human heart organoids using optical coherence tomography," Biosensors and Bioelectronics **207**, 114136 (2022).
25. S. Hao, C. Ren, F. Wang, K. Park, B. D. Volmert, A. Aguirre, and C. Zhou, "Dual-modality imaging system for monitoring human heart organoids beating in vitro," Optics Letters **48**, 3929-3932 (2023).
26. M. Kvåle Løvmo, S. Deng, S. Moser, R. Leitgeb, W. Drexler, and M. Ritsch-Marte, "Ultrasound-Induced Reorientation for Multi-Angle Optical Coherence Tomography," bioRxiv, 2023.2010. 2004.560819 (2023).
27. A. J. Deloria, S. Haider, B. Dietrich, V. Kunihs, S. Oberhofer, M. Knöfler, R. Leitgeb, M. Liu, W. Drexler, and R. Haindl, "Ultra-high-resolution 3D optical coherence tomography reveals inner structures of human placenta-derived trophoblast organoids," IEEE Transactions on Biomedical Engineering **68**, 2368-2376 (2020).
28. S. Pi, A. Camino, M. Zhang, W. Cepurna, G. Liu, D. Huang, J. Morrison, and Y. Jia, "Angiographic and structural imaging using high axial resolution fiber-based visible-light OCT," Biomedical optics express **8**, 4595-4608 (2017).
29. X. Zhong, C. Gutierrez, T. Xue, C. Hampton, M. N. Vergara, L.-H. Cao, A. Peters, T. S. Park, E. T. Zambidis, and J. S. Meyer, "Generation of three-dimensional retinal tissue with functional photoreceptors from human iPSCs," Nature communications **5**, 4047 (2014).
30. C. S. Cowan, M. Renner, M. De Gennaro, B. Gross-Scherf, D. Goldblum, Y. Hou, M. Munz, T. M. Rodrigues, J. Krol, and T. Szikra, "Cell types of the human retina and its organoids at single-cell resolution," Cell **182**, 1623-1640. e1634 (2020).
31. M. A. Branco, J. P. Cotovio, C. A. Rodrigues, S. H. Vaz, T. G. Fernandes, L. M. Moreira, J. M. Cabral, and M. M. Diogo, "Transcriptomic analysis of 3D cardiac differentiation of human induced pluripotent stem cells reveals faster cardiomyocyte maturation compared to 2D culture," Scientific reports **9**, 9229 (2019).
32. W. Feng, H. Schriever, S. Jiang, A. Bais, H. Wu, D. Kostka, and G. Li, "Computational profiling of hiPSC-derived heart organoids reveals chamber defects associated with NKX2-5 deficiency," Communications Biology **5**, 399 (2022).
33. O. Ronneberger, P. Fischer, and T. Brox, "U-net: Convolutional networks for biomedical image segmentation," in *Medical Image Computing and Computer-Assisted Intervention–MICCAI 2015: 18th International Conference, Munich, Germany, October 5-9, 2015, Proceedings, Part III 18*(Springer2015), pp. 234-241.
34. J. Fu, J. Liu, H. Tian, Y. Li, Y. Bao, Z. Fang, and H. Lu, "Dual attention network for scene segmentation," in *Proceedings of the IEEE/CVF conference on computer vision and pattern recognition*(2019), pp. 3146-3154.
35. W. Wang, S. Wang, Y. Li, and Y. Jin, "Adaptive multi-scale dual attention network for semantic segmentation," Neurocomputing **460**, 39-49 (2021).
36. R. Rasti, A. Biglari, M. Rezapourian, Z. Yang, and S. Farsiu, "RetiFluidNet: A Self-Adaptive and Multi-Attention Deep Convolutional Network for Retinal OCT Fluid Segmentation," IEEE Transactions on Medical Imaging (2022).
37. Z. Lin, Z. He, R. Yao, X. Wang, T. Liu, Y. Deng, and S. Xie, "Deep dual attention network for precise diagnosis of covid-19 from chest ct images," IEEE Transactions on Artificial Intelligence (2022).
38. L.-C. Chen, Y. Zhu, G. Papandreou, F. Schroff, and H. Adam, "Encoder-decoder with atrous separable convolution for semantic image segmentation," in *Proceedings of the European conference on computer vision (ECCV)*(2018), pp. 801-818.

39. R. Ganjee, M. Ebrahimi Moghaddam, and R. Nourinia, "A generalizable approach based on the U-Net model for automatic intraretinal cyst segmentation in SD-OCT images," International Journal of Imaging Systems and Technology (2023).
40. Z. Yang, S. Soltanian-Zadeh, and S. Farsiu, "BiconNet: An edge-preserved connectivity-based approach for salient object detection," Pattern recognition **121**, 108231 (2022).
41. A. W. Browne, C. Arnesano, N. Harutyunyan, T. Khuu, J. C. Martinez, H. A. Pollack, D. S. Koos, T. C. Lee, S. E. Fraser, and R. A. Moats, "Structural and functional characterization of human stem-cell-derived retinal organoids by live imaging," Investigative ophthalmology & visual science **58**, 3311-3318 (2017).
42. D. A. Gil, D. A. Deming, and M. C. Skala, "Volumetric growth tracking of patient-derived cancer organoids using optical coherence tomography," Biomedical Optics Express **12**, 3789-3805 (2021).
43. T. Monfort, S. Azzollini, J. Brogard, M. Clémençon, A. Slembrouck-Brec, V. Forster, S. Picaud, O. Goureau, S. Reichman, and O. Thouvenin, "Dynamic full-field optical coherence tomography module adapted to commercial microscopes allows longitudinal in vitro cell culture study," Communications Biology **6**, 992 (2023).
44. Y. Huang, S. Wang, Q. Guo, S. Kessel, I. Rubinoff, L. L.-Y. Chan, P. Li, Y. Liu, J. Qiu, and C. Zhou, "Optical coherence tomography detects necrotic regions and volumetrically quantifies multicellular tumor spheroids," Cancer research **77**, 6011-6020 (2017).
45. H. Clevers, "Modeling development and disease with organoids," Cell **165**, 1586-1597 (2016).
46. T. A. Afanasyeva, J. C. Corral-Serrano, A. Garanto, R. Roepman, M. E. Cheetham, and R. W. Collin, "A look into retinal organoids: methods, analytical techniques, and applications," Cellular and Molecular Life Sciences **78**, 6505-6532 (2021).
47. P. Mladěnka, L. Applová, J. Patočka, V. M. Costa, F. Remiao, J. Pourová, A. Mladěnka, J. Karlíčková, L. Jahodář, and M. Vopršalová, "Comprehensive review of cardiovascular toxicity of drugs and related agents," Medicinal research reviews **38**, 1332-1403 (2018).
48. R. Gong, Z. Jiang, N. Zagidullin, T. Liu, and B. Cai, "Regulation of cardiomyocyte fate plasticity: a key strategy for cardiac regeneration," Signal Transduction and Targeted Therapy **6**, 31 (2021).
49. S. E. Park, A. Georgescu, and D. Huh, "Organoids-on-a-chip," Science **364**, 960-965 (2019).